Airborne measurements and large-eddy simulations of small-scale Gravity Waves at the tropopause inversion layer over Scandinavia

Sonja Gisinger[1], Johannes Wagner[1], and Benjamin Witschas[1]

[1]Deutsches Zentrum für Luft- und Raumfahrt, Institut für Physik der Atmosphäre, Oberpfaffenhofen, Germany

Correspondence: Sonja Gisinger (sonja.gisinger@dlr.de)

Abstract. Coordinated airborne measurements were performed by the two research aircraft DLR Falcon and HALO (High Altitude and Long Range Aircraft) in Scandinavia during the GW-LCYCLE II (Investigation of the life cycle of gravity waves) campaign in 2016 to investigate gravity wave processes in the upper troposphere and lower stratosphere (UTLS) region. A mountain wave event was probed over Southern Scandinavia on 28 January 2016. The collected dataset constitutes a valuable combination of in-situ measurements and horizontal- and altitude-resolved wind lidar and water vapour lidar measurements. In-situ data at different flight altitudes and downward pointing Doppler wind lidar measurements show pronounced changes of the horizontal scales in the vertical velocity field and of the leg-averaged momentum fluxes (MF) in the UTLS region. The vertical velocity field was dominated by small horizontal scales with a decrease from around $20\,\mathrm{km}$ to $<10\,\mathrm{km}$ in the vicinity of the tropopause inversion layer (TIL). These small scales were also found in the water vapour and reflectivity data. The MF profile downstream of the main mountain ridge determined from the wind lidar data is characterized by negative fluxes below and positive fluxes above the TIL which show similar magnitudes. The combination of the observations and idealized large-eddy simulations (LES) revealed the occurrence of interfacial waves on the tropopause inversion during the MW event. Such interfacial waves have already been observed on boundary-layer inversions but their concept has not been applied to tropopause inversions so far. Our idealized simulations revealed that interfacial waves can occur also on tropopause inversions and our analyses of the horizontal- and altitude-resolved airborne observations revealed that they actually do. As predicted by linear theory, the horizontal scale of those waves is determined by the wind and stability conditions above the inversion. They are found downstream of the main mountain peaks and their characteristic MF profile clearly distinguishes from the MF profile of a Kelvin-Helmholtz instability. Further, the idealized large-eddy simulations revealed that the presence of the TIL is crucial in producing this kind of trapped waves at tropopause altitude.

1 Introduction

Gravity waves (GWs) are an important coupling mechanism between the lower and the middle and upper atmosphere. Propagating GWs transport momentum and energy and deposit them in regions where breaking and dissipation occurs. As such, GWs account for example for the well known upper mesospheric wind reversals as well as the cold polar summer mesopause and the warm winter stratopause (Dunkerton, 1978; Lindzen, 1981). So far, different sources for GWs in the troposphere have been identified, e.g., flow over orography, convection, jets and fronts as well as secondary generation in the region of GW

breaking (Smith, 1979; Gill, 1982; Baines, 1995; Fritts and Alexander, 2003; Sutherland, 2010; Plougonven and Zhang, 2014; Vadas et al., 2003). Turbulence caused by breaking GWs and wave-induced modulations of the ambient wind can be hazards to aviation in the troposphere and lower stratosphere (Sharman et al., 2012; Bramberger et al., 2018). GWs are propagating from their sources in the troposphere and the tropopause region (Sato et al., 2009; Fritts et al., 2016). However, the atmospheric

30 temperature and wind structures influence the propagation of GWs and alter their properties. The vertical distance from the lower troposphere to the most prominent breaking region around the mesopause is about 70 km where changes in wind and temperature occur (Eckermann, 1995; Doyle and Jiang, 2006; Eckermann et al., 2007).

Since the works of Queney (1948) and Scorer (1949), different theoretical and numerical methods were used to study mountain wave (MW) propagation in an atmosphere of vertically varying wind and stability. Those methods are ray tracing,

35 determination of reflection and transmission coefficients, numerical solutions of the vertical structure equation for single wave components, analytical models, and asymptotic analysis (see Wurtele et al. (1987) and references therein, and more recently, Eckermann and Marks (1997); Gisinger et al. (2017); Achatz et al. (2010)). An important result of the theoretical investigations is that the stratospheric solution in a model taking into account a vertically varying background is not dominated by the classical solution of Queney (1948) but by reflected and downstream propagating (trapped) waves in the troposphere (Wurtele et al.,

40 1987; Keller, 1994). This makes the wave spectrum (i.e. wavelengths) being determined by the vertical varying wind and stability and not by the topography spectrum which affects the relative amplitudes (Keller, 1994; Ralph et al., 1997). Fine scale structures in the atmosphere, such as sharp temperature inversions at the top of the boundary layer (Vosper, 2004; Sachsperger et al., 2015) or in the mesosphere (Fritts et al., 2018) can be wave guides leading to trapped waves which propagate horizontally along the inversions, i.e. interfacial waves. All those findings are in contrast to the fundamental characteristics of the hydrostatic

45 approximation. They are the absence of a mechanism which allows a wave to propagate horizontally and the consequent upward propagation of energy directly above the obstacle, regardless of the generating terrain (Wurtele et al., 1996).

Currently much activity using various ground-based, airborne, and satellite measurements is going on to get a complete picture of the GW activity and distribution around the globe and to enhance the understanding of source and propagation processes (e.g., Fritts et al., 2016; Podglajen et al., 2016; Wright et al., 2017; Shibuya et al., 2017; Kaifler et al., 2017; Krisch

50 et al., 2017). This knowledge is required to adequately model and parameterize atmospheric GWs in weather and climate models. So far, observational indications of GW behaviour in the tropopause region such as reflection and trapping are rare due to lack of horizontal- and altitude-resolved observations in the tropopause region. Using aircraft measurements, which were taken during the Terrain-Induced Rotor Experiment (T-REX, Grubišić et al. (2008)), Smith et al. (2008) were able use in-situ data to measure partial reflection of MWs at the tropopause for the first time. Using their linear model, they identified two levels

55 of reflection, one at the altitude where the Scorer parameter changes due to changes in static stability and the other at the altitude with a discontinuity in wind speed but constant Scorer parameter. In addition, Smith et al. (2008) and Woods and Smith (2010) found signatures of trapped waves with a horizontal wavelength of about 15 km in the in-situ measurements in the tropopause inversion layer (TIL) during T-REX. They argue that the Sierra mountain range is unlikely to be the source for those 15-km waves. They do not expect those waves to reach the tropopause altitude from below because the background conditions caused

60 a considerable evanescent decay. Instead, they suggest that those waves were generated by a nonlinear steepening process.

Follow-up model simulations lead to two different explanations. First, the short-wavelike fluctuations observed in the UTLS region are due to Kelvin-Helmholtz instability along shear lines locally induced by the primary mountain wave, i.e. they are not trapped GWs but instead small-scale wave motions resulting from Kelvin-Helmholtz instability (Mahalov et al., 2011). Second, the downward propagating GWs, which are created by MW breaking in the middle stratosphere, and their reflection at the tropopause can create kind of lee wave trapping in the lower stratosphere (Woods and Smith, 2011).

Coordinated airborne measurements were performed by the two research aircraft DLR Falcon and HALO (High Altitude and Long Range Aircraft) in Scandinavia during the GW-LCYCLE II (Investigation of the life cycle of gravity waves) campaign in 2016 to investigate GW processes in the upper troposphere and lower stratosphere (UTLS) region. A mountain wave event was probed over Southern Scandinavia on 28 January 2016. The collected dataset constitutes a valuable combination of in-situ measurements and horizontal- and altitude-resolved wind lidar and water vapour lidar measurements in the UTLS. In-situ data at different flight altitudes and downward pointing Doppler wind lidar measurements revealed pronounced changes of the horizontal scales in the vertical velocity field and of the leg-averaged momentum fluxes (MF) in the UTLS region.

This paper examines the MW case over Scandinavia by means of ECMWF IFS meteorological analyses and the coordinated airborne measurements of the DLR Falcon and HALO which provide horizontal- and altitude-resolved data in the UTLS. The wind data of the downward pointing Doppler lidar give the opportunity to calculate a continuous profile of MF over a two-kilometer altitude range in the UTLS. In order to find out what determines the horizontal scales in the vertical velocity field and which process(es) can explain the observed characteristics, we investigate the possible existence of interfacial waves on the TIL (Vosper, 2004; Sachsperger et al., 2015, 2017) similar to their existence on an inversion in the troposphere (Cruette, 1976; Sachsperger et al., 2015; Chouza et al., 2015). The paper is organized as follows. Section 2 describes the models, data and methods used in this paper. Meteorological conditions and observations of the MW event on 28 January 2016 are analyzed in Section 3.1 and idealized large-eddy simulations of MW propagation in the presence of atmospheric inversions are presented in Section 3.2. Section 4 gives a tight discussion of the results and Section 5 concludes the paper.

2 Data and Methods

2.1 ECMWF global analysis

Operational analyses of the ECMWF integrated forecast system (IFS) are used to analyse the meteorological conditions on 28 January 2016. These analyses (cycle 41r1[1]) have a horizontal resolution of about 16 km on the reduced linear Gaussian grid (T_L 1279). The highest of the 137 vertical levels (L137) is located at ~ 80 km (0.01 hPa). The layer thicknesses gradually increases from ~ 300 m at ~ 10-km altitude to ~ 400 m at ~ 20-km altitude and ~ 2 km at ~ 60-km altitude[2].

---

[1]https://www.ecmwf.int/en/forecasts/documentation-and-support/changes-ecmwf-model/cy41r1-summary-changes, last access Oct 2018

[2]https://www.ecmwf.int/en/forecasts/documentation-and-support/137-model-levels, last access Oct 2018

2.2 Airborne observations

2.2.1 Coordinated research flights on 28 January 2016

90

The airborne observations took place during the intensive observing period 6 (IOP 6) on 28 January 2016 in the framework of the combined missions POLSTRACC (The Polar Stratosphere in a Changing Climate), GW-LCYCLE II and SALSA (Seasonality of Air mass transport and origin in the Lowermost Stratosphere using the HALO Aircraft). An overview of the performed HALO research flights can be found in Oelhaf et al. (2019). In January 2016, the DLR research aircraft Falcon and HALO

95 operated from the airport of Kiruna (67.82° N, 20.33° E), northern Sweden, to investigate chemical and dynamical processes in the UTLS region at high latitudes. The goal of IOP 6 was to measure a transient MW event over southern Scandinavia with coordinated cross-mountain flights of both aircraft. Figure 1a shows the operational area and the flight tracks of the research flights. The mountains were crossed at the same latitude two times by the DLR Falcon (flight legs RF07 FL2 and RF08 FL1) and three times by HALO (flight legs HL1, HL2 and HL4; Fig.1b). The limited range of the DLR Falcon required a refuel stop

100 at Karlstad airport. The DLR Falcon was flying close to the thermal tropopause on all flight legs and measured vertical winds and GW induced momentum fluxes with the in-situ sensor at flight altitude and with the downward pointing Doppler wind lidar below the aircraft. On the flight legs HL1 and HL2 HALO was flying in the troposphere (HL1 below the DLR Falcon) and measured wave structures at flight level and in the tropopause region with the upward pointing differential absorption lidar (DIAL) measuring water vapour (WALES) (Wirth et al., 2009).

2.2.2 Wind lidar measurements

105

The DLR Falcon was among others equipped with a downward-looking coherent Doppler wind lidar (DWL) which has been operated by DLR since 1999 and which has been applied in a number of field campaigns (e.g., Chouza et al., 2017; Schäfler et al., 2018; Marksteiner et al., 2018; Lux et al., 2018). The DWL operates at a wavelength of 2 μm and is equipped with a double-wedge scanner which enables to steer the laser beam to any position within a cone angle of 30°. A more detailed

110 description of the 2 μm DWL instrumental setup, the measurement principle, the applied retrieval algorithms and the accuracy and precision of the derived wind products is given by Chouza et al. (2015), Witschas et al. (2017), and more recently Witschas et al. (2020).

Usually, the 2 μm DWL is used to either measure the three dimensional wind vector by applying the velocity azimuth display (VAD) scan technique, or to measure vertical wind speeds by pointing the laser beam to nadir direction and compensate

115 any attitude changes of the aircraft by means of the double wedge scanner. As shown and discussed by Witschas et al. (2017), measurements of both horizontal and vertical wind profiles are very useful to characterize the spectral properties of mountain waves. In order to additionally gain knowledge of the momentum transport of mountain waves, horizontal wind speed (u) and vertical wind speed (w) need to be measured simultaneously. The leg-averaged momentum flux ($\propto \overline{u'w'}$) can then be calculated like in Smith et al. (2016). Here, $'$ denotes perturbations of the respective quantity. For this purpose, the 2 μm DWL has been

120 operated with a modified scan pattern during the GW-LCYCLE II campaign for the first time. In particular, the laser beam has alternately been steered forth and back with an off-nadir angle of ±20°. With that and the knowledge of the laser beam

pointing direction, u and w can be derived from a successive pair of line-of-sight (LOS) measurements. It is worth mentioning that u denotes the horizontal wind along flight direction here, which coincided well with the wind direction for the discussed flight (see section 3.1.1).

125   For the applied scan pattern, each LOS measurement took 2 s and the aircraft speed above ground was approximately 200 m s^{-1}. Thus, the horizontal resolution of the measured horizontal and vertical wind is ≈ 800 m. A more detailed explanation of the momentum-flux scan pattern of the 2 μm DWL will be presented in Witschas et al. (in preparation).

2.2.3   In-situ measurements

Horizontal and vertical velocity data at flight level are provided by the DLR facility Flight Experiments. For the DLR Falcon,
130 the velocity field is determined from data taken by a Rosemount model 858 flow angle sensor and a Honeywell Lasernav YG 1779 inertial reference system (IRS) (Bögel and Baumann, 1991). Measurements on HALO are conducted by the Basic HALO Measurement and Sensor System (BAHAMAS). Recent method and calibration details can be found in Mallaun et al. (2015) and Giez et al. (2017). For the horizontal wind the measurement uncertainties are smaller than 0.5 m s^{-1} for HALO and 0.9 m s^{-1} for Falcon, and smaller than 0.3 m s^{-1} for the vertical wind (Heller et al., 2017; Bramberger et al., 2018). The
135 data are used at a time resolution of 1 s. Perturbation quantities of the velocity data (u', v', w') are calculated by de-trending the data with a linear least square fit and subtracting the mean over the leg (Portele et al., 2018). Wavelet spectra of vertical velocity and MF cospectra of $\rho u' w'$ (Woods and Smith, 2010) with modifications of Portele et al. (2018) are computed based on Torrence and Compo (1998)[3].

2.3   Idealized numerical simulations

140 EULAG[4] is a multi-scale computational model for the simulation of geophysical flows. It provides at least second-order accuracy in time and space (Prusa et al., 2008). EULAG solves the governing equations of motion either in an EUlerian or a LAGrangian form. Here, the non-hydrostatic equations of motion

$$\frac{D\mathbf{v}}{Dt} = -\nabla \frac{p'}{\bar{\rho}} + \mathbf{g}\frac{\theta}{\bar{\theta}} - \mathbf{f} \times \mathbf{v}' + \mathcal{M}', \tag{1}$$

$$\frac{D\theta}{Dt} = 0, \tag{2}$$

145   $\nabla \cdot (\bar{\rho}\mathbf{v}) = 0, \tag{3}$

are used in their Boussinesq approximated ($\bar{\rho} = \rho_0$) form for the first set of simulations and decrease of density with altitude is taken into account for the second set of simulations (Smolarkiewicz et al., 2001; Prusa et al., 2008). $\frac{D}{Dt}$ is the material derivative, $\mathbf{v}$ is the velocity vector, p is pressure, ρ is density, θ is potential temperature, $\mathcal{M}$ represents appropriate metric forces, and $\mathbf{f}$ and $\mathbf{g}$ symbolize the vectors of Coriolis parameter and gravity acceleration. Primes denote deviations from the
150 ambient state and overbars refer to the horizontally homogeneous hydrostatic reference state of the Boussinesq expansion

---

[3]Wavelet software was provided by C. Torrence and G. Compo, and is available at URL: http://atoc.colorado.edu/research/wavelets/, last access Nov 2019
[4]http://www2.mmm.ucar.edu/eulag/, last access Nov 2019

around a constant stability profile (Smolarkiewicz et al., 2001). EULAG has been applied for a broad range of topics in fluid dynamics including orographic GWs (e.g., Prusa et al., 1996; Grubišić and Smolarkiewicz, 1997). Detailed model setup is given in Section 3.2.

3 Results

3.1 MW event over Southern Scandinavia

3.1.1 Meteorological situation

IOP 6 was a transient MW event over southern Scandinavia on 28 January 2016. Two synoptic low pressure systems over the tip of Greenland and over the Baltic sea caused moderate south-westerly to westerly winds ($10 \, \mathrm{m \, s^{-1}}$ to $20 \, \mathrm{m \, s^{-1}}$) in the troposphere and the excitation of MWs at the Southern Scandinavian mountain range (Fig. 2a). At tropopause level ($300 \, \mathrm{hPa}$) winds were westerly and below $30 \, \mathrm{m \, s^{-1}}$ over Southern Scandinavia as the polar front jet was located over the British Isles and northern Germany. A secondary jet streak occurred over the Norwegian Sea between Iceland and the Norwegian coast (Fig. 2b). The vertical cross section of horizontal wind speed interpolated in time and space along flight leg RF08 FL2 shows increasing wind speed up to $80 \, \mathrm{m \, s^{-1}}$ above 20-km altitude in the stratosphere (Fig 3a). The cross section of vertical wind shows vertically propagating MWs in the troposphere and increasing wave amplitudes in the stratosphere (Fig 3b). The resolved MWs in ECWMF are associated with the main mountain peaks of the IFS model topography.

In Fig. 4, a time-height section of ECMWF horizontal wind speed located at the mountain ridge at point X_0 (Fig. 1a) is plotted. MWs were generated by moderate wind speeds in the lower troposphere on 28 January 2016. However, the MWs were prevented from propagating into the stratosphere until about 8 UTC due to weak winds close to $0 \, \mathrm{m \, s^{-1}}$ in the mid-troposphere. After 10 UTC, wind speeds above the tropopause and in the mid-troposphere increased which have allowed vertical propagation of tropospheric GWs into the stratosphere. During the time of the research flights (red dots in Fig. 4), wind speeds below the tropopause weakened again ($10 \, \mathrm{m \, s^{-1}}$-$15 \, \mathrm{m \, s^{-1}}$).

Vertical profiles of horizontal wind speed and Brunt-Vaisala frequency from an operational sounding[5] started from Stavanger (Fig. 1) at 12 UTC on 28 January 2016 are shown in Fig. 5a, b. This figure illustrates the moderate winds in the troposphere, the pronounced jump in static stability at the tropopause, that is typical for a TIL (Birner, 2006), and the increasing winds with height in the stratosphere within the polar vortex. The critical horizontal wavelength which separates evanescent and propagating GWs was mainly larger than $10 \, \mathrm{km}$ in the troposphere (i.e. only waves with horizontal wavelength $> 10 \, \mathrm{km}$ can propagate), smaller than $10 \, \mathrm{km}$ in the vicinity of the TIL, and increasing towards $20 \, \mathrm{km}$ above in the stratosphere (Fig. 5c).

3.1.2 Airborne observations

The coordinated flights of HALO and DLR Falcon provided simultaneous measurements of GW induced perturbations below and in the TIL. Figure 6a shows vertical velocities observed at flight level on all 5 cross mountain flight legs. Amplitudes of

---

[5]sounding data from http://weather.uwyo.edu/upperair/

$2\,\mathrm{m\,s^{-1}}$ in the troposphere and up to $4\,\mathrm{m\,s^{-1}}$ in the stratosphere are visible on all legs. Tropospheric measurements (HL1, HL2) show longer horizontal wavelengths compared to the observations at tropopause altitudes (RF07 FL2, RF08 FL1), which means that GW properties change in the vicinity of the tropopause. Wavelet power spectra of the observed vertical winds were computed to analyse the change in horizontal wavelengths (Fig. 6b). Wavelengths in the troposphere were in the order of $10\,\mathrm{km}$

185 to $30\,\mathrm{km}$ (PGS11 HL1 and HL2), while wavelet analysis shows that shorter wavelengths of $5\,\mathrm{km}$ to $9\,\mathrm{km}$ are dominating for RF07 FL2 and RF08 FL1 in downstream region. Longer waves with wavelengths of ≥ 10 km are found for the uppermost flight leg in the lower stratosphere (PGS11 HL4). Note that this was the last flight leg and it took place about two hours later than the other flight legs. The revealed wave signatures are not directly related to the topography spectrum (Fig. 6b) which was computed from the ASTER topography data (Schmugge et al., 2003) along the flight track (shown in Fig. 6a). The wave

190 signatures are influenced by the background conditions.

Wavelet cospectra of MF were computed to study the propagation characteristics of the waves in more detail (Fig. 7). Alternating positive and negative MF at wavelengths of $10\,\mathrm{km}$ to $30\,\mathrm{km}$ were observed at distances of $-100\,\mathrm{km}$ to $0\,\mathrm{km}$ and $100\,\mathrm{km}$ to $300\,\mathrm{km}$ below and in the tropopause region on the flight legs which took place at nearly the same time (PGS11 HL1 and HL2, RF08 FL1). This alternating pattern is an indication for reflected and trapped waves. Significant MF at shorter

195 wavelengths is found in the tropopause region and strongest alternating positive and negative signals occur downstream of the main mountain peaks. No significant positive or negative MF is found for the short scales < 10 km above the tropopause at 13 km altitude (PGS11 HL4). These findings indicate that the short waves are trapped in the tropopause region. Upward propagating longer waves (negative MF) with horizontal wavelengths of approximately $40\,\mathrm{km}$ to $50\,\mathrm{km}$ are found for RF08 FL1 and PGS11 HL4 at $120\,\mathrm{km}$ distance.

200 The DLR Falcon DWL measured in nadir mode on the first cross-mountain flight leg RF07 FL2 (Fig. 8). Measured vertical winds show fine scale up- and downdrafts over the mountains. The horizontal wavelengths of the GWs are smaller downstream of X_0 on the lee side of the mountain and the phase lines are vertical. This again indicates wave trapping.

Lidar and in-situ measurements of the coordinated flight legs RF08 FL1 and PGS11 HL1 are shown in Fig. 9. As the DWL of DLR Falcon operated in flux mode on this leg, both the horizontal wind component in flight direction and the vertical wind

205 component were measured. Contour lines of lidar measurements are overlaid by in-situ wind measurements of both aircraft. Wind measurements are complemented by water vapour measurements of the upward looking DIAL of HALO. Horizontal wind speeds in Fig. 9a show large scale wave structures with upstream tilted phase lines in the troposphere. In-situ measurements around the tropopause indicate similar wave structures but with stronger wind speeds compared to tropospheric values. In addition, large-scale wave structures are superimposed by small-scale waves with vertical phase lines. These small scale-

210 waves are more clearly visible in vertical wind measurements, which are more sensitive to smaller scale waves (Lane et al., 2003; Smith and Kruse, 2017), and show a clear change from longer to smaller wavelengths below and in the vicinity of the tropopause (Fig. 8 and 9b). This behaviour was already revealed by the wavelet analysis of the in-situ measurements (Fig. 6b). The short horizontal wavelengths are also visible in observations of water vapour mixing ratio (Fig. 9c) and the lidar reflectivity (Fig. 9d) between $8\,\mathrm{km}$ and $10\,\mathrm{km}$ altitude.

215 Additional information regarding the wave propagation comes with the direct measurements of GW induced momentum fluxes by the new momentum flux method of the Falcon DWL. This was done on the coordinated flight leg RF08 FL1. Figure 10 illustrates vertical profiles of leg-averaged momentum fluxes along the cross-mountain flight legs RF08 FL1, PGS11 HL1 and HL4 obtained from lidar and in-situ measurements. The leg is split into an upstream part (segment 1), a part above the main mountain range (segment 2), and a part downstream of the main mountain range (segment 3). The profile of segment 3 indicates

220 upward propagating (negative momentum fluxes) below 8 km altitude and downward propagating (positive momentum fluxes) around the tropopause. This suggests that waves were reflected and trapped in the vicinity of the TIL. Leg averaged in-situ momentum fluxes show upward propagating waves above the 9.5-km altitude over the main mountain range (segment 2). The measured MF profile in the downstream region (Figs. 10) does not match the typical profile of a Kelvin-Helmholtz instability that is characterised by one peak of positive MF (Mahalov et al., 2011).

3.2 Idealized simulations of MWs and the TIL

In this section, it is investigated if interfacial waves on an inversion found in the lower troposphere can also occur at tropopause altitudes and which conditions are necessary for their occurrence. It is tested if this wave trapping was possible on 28 January 2016 over southern Scandinavia by performing additional 2-dimensional simulations with the Scandinavian topography and background profiles which approximate the prevailing conditions on 28 January 2016. There is no intention to tune the

230 simulations as close to the measurements as possible because the main goal in this study is to identify processes which could explain the observed wave structure in the UTLS.

The computational parameters are chosen similar to Vosper (2004) for the first set of simulations. The 2-dimensional domain consists of 1032 and 2000 grid points in x- and z-direction, respectively, with grid increments of $\Delta x = 100$ m and $\Delta z = 10$ m (terrain following). This results in a total domain size of about 103 km $\times$ 20 km. The integration time step Δt is set to 1 s. Open

235 boundaries are applied in x-direction. The model top is a rigid lid. The sponge layers at the horizontal edges of the domain are 8 km wide and the sponge layer at the top of the domain starts at 15-km altitude. As in Vosper (2004) an idealized ridge

$$
h(x) = \begin{cases} h_0[1 + \cos(Kx)]/2 & \text{for } |x| \leq \pi/K \\ 0 & \text{for } |x| > \pi/K, \end{cases}
\tag{4}
$$

where $K = 2\pi/L$, and free slip lower boundary condition are used. Mountain height h_0 is set to 400 m and width L to 10 km or 5 km. The usage of this idealized ridge is considered to be sufficient to investigate the occurrence and changes in the

240 horizontal scale of the GWs in the vicinity of the TIL because it is known that the horizontal wavelength of interfacial waves is independent of the mountain half-width and height (Sachsperger et al., 2017). Four simulations are performed with a vertically constant horizontal velocity $U = 8 \text{ m s}^{-1}$ and different profiles of potential temperature with the corresponding Brunt-Väisälä frequency as initial conditions. Table 1 summarizes the relevant initial parameters of the different model runs.

Figure 11a, b (RUN 1 and 2) shows that the EULAG model can reproduce the findings of Vosper (2004): an inversion

245 at the top of an neutral boundary layer leads downstream propagating waves at the altitude of the inversion (Fig. 11b). The horizontal wavelength is approximately 5 km and the largest amplitudes are found in the vicinity of the inversion (Fig. 12c).

The signal is weak below the inversion (Fig. 12d) and absent if no inversion is present (Fig. 12a, b). If the stability above the inversion is increased to $N_U = 0.02\,\mathrm{s}^{-1}$ (stratospheric stability), the strength of the inversion $\Delta\theta$ must be twice as large to allow for wave trapping and horizontal propagation on the inversion (RUN 3). The horizontal wavelength of the interfacial waves

250   decreases with increasing stability above the inversion. The horizontal wavelength is approximately 2.5 km for $U = 8\,\mathrm{m\,s}^{-1}$ and $N_U = 0.02\,\mathrm{s}^{-1}$ (Fig. 12f). This is because for $N_U = 0.02\,\mathrm{s}^{-1}$ waves with a horizontal wavelength of 5 km are no longer evanescent above the inversion and can propagate vertically (no trapping). The vertical profile of MF associated with the interfacial waves on the boundary layer inversion downstream of the idealized mountain (Fig. 11b, Fig. 12c) is shown in Fig. 13. Negative and positive MF of same magnitude are found below and above the inversion, respectively. This MF profile

255   differs from the MF profile of a Kelvin-Helmholtz instability for which MF is zero below and above the instability (Mahalov et al., 2011).

Figures 11d and 12h (RUN 4) show that interfacial waves can also exist on the TIL located between a stably stratified troposphere ($N_L = 0.01\,\mathrm{s}^{-1}$) and the stratosphere ($N_U = 0.02\,\mathrm{s}^{-1}$). The horizontal wavelength is again approximately 2.5 km for $U = 8\,\mathrm{m\,s}^{-1}$. Besides the upward propagating MWs and the interfacial waves, reflected waves with a horizontal wavelength

260   of approximately 5 km exist downstream of the mountain in the troposphere (Figs. 11d and 12j) although the classical trapping condition of a decreasing Scorer parameter with altitude in the troposphere (Scorer, 1949) is not fulfilled. The amplitudes of the reflected waves are found to be larger if an inversion is present at the tropopause than if there is just the jump from tropospheric to stratospheric stability (not shown). The results of these numerical simulations confirm that interfacial waves can exist on the TIL. The mechanism of their trapping (evanescence in the layer above the inversion), the resulting horizontal wavelength,

265   and the occurring horizontal propagation match the published results for boundary-layer inversions (Vosper, 2004; Sachsperger et al., 2015).

The second set of simulations (RUN 5 and 6) uses a 2-dimensional domain with 2016 and 1000 grid points in x- and z-direction, respectively, with grid increments of $\Delta x = 500$ m and $\Delta z = 40$ m. This results in a total domain size of about 1008 km × 40 km. The integration time step Δt is set to 1 s. Open boundaries are applied in x-direction. The model top is a

270   rigid lid. The sponge layers at the horizontal edges of the domain are 40 km wide and the sponge layer at the top of the domain starts at 25 km altitude. The Scandinavian topography is interpolated on the 500 m grid from ASTER data. The initial profiles approximate the background conditions over Southern Scandinavia given by the Stavanger radiosonde on 28 January 2016 (Fig. 14a, b, d, e). Simulations without and with a TIL are performed. The simplified initial horizontal velocity profile does not contain negative shear above the tropopause but negative shear establishes in the course of the simulation (black dashed

275   profiles shown in Fig. 14a, d are located at -150 km distance (Fig. 15f) 16 hours after start of the simulations).

Figures 14f and 15h (RUN 6) show that interfacial waves can also exist for the background conditions found on 28 January 2016 over Southern Scandinavia. They are found downstream of the main mountain peak in the vicinity of the TIL (Fig. 14f and Fig. 15f) and their horizontal wavelength is approximately 8 km (Fig. 15h). The horizontal band pattern in the wavelet spectrum resembles the one of the idealized mountain simulations presented above (Fig. 12c, f, h). Interfacial small

280   scale waves are absent in the troposphere below the TIL (Fig. 15i) and in the case of no TIL (RUN 5, Fig. 14c and Fig. 15a, c). Reflected waves with horizontal wavelengths between 10 km and 30 km exist downstream of the main mountain peaks in the

troposphere (Figs. 14c, f and 15d, i). It was already mentioned that the horizontal wavelength of the interfacial waves is independent of the generating terrain and determined by the background wind and stability. These 2-dimensional simulations reveal the expected wavelength of the GWs over Southern Scandinavia downstream of the main mountain ridge on 28 January 2016, i.e. approximately 8 km in the vicinity of the TIL and between 10 km and 30 km in the troposphere. However, the interfacial waves in the simulation are not as dominant as in the measurements (Fig. 15h vs. RF07 FL2 and RF08 FL1 in Fig. 6b). There is a stronger signal of the upward propagating MWs above the main mountain peaks (Fig. 15f, h).

4 Discussion

The atmospheric conditions during the MW case were characterized by moderate low level flow ($\sim 10\ \mathrm{m\,s^{-1}}$), comparatively weak wind speed ($\sim 30\ \mathrm{m\,s^{-1}}$) around the TIL and increasing wind speed above (Sec. 3.1.1). The coordinated airborne measurements including the downward pointing Doppler wind lidar measurements revealed that the vertical velocity field was dominated by small horizontal scales with a decrease from around 20 km to < 10 km in the vicinity of the TIL. These small scales were also found in the water vapour and reflectivity data (Sec. 3.1.2). The corresponding MF indicates wave reflection and trapping at the TIL (Fig. 7 and Fig. 10). It is known that atmospheric inversions can be wave guides leading to wave trapping and downstream wave propagation (Vosper, 2004; Sachsperger et al., 2015; Chouza et al., 2015; Fritts et al., 2018) but observations of downstream wave propagation of small scale waves at tropopause inversions are rare (Smith et al., 2008; Woods and Smith, 2010).

In the course of investigating MW propagation in the UTLS with horizontal- and altitude-resolved airborne observations (Section 3.1.2), we found that the measured and simulated MF profiles downstream of the main mountain ridge (Figs. 10 and 13) do not match the typical profile of a Kelvin-Helmholtz instability (Mahalov et al., 2011). The shear was not strong enough to generate Kelvin-Helmholtz instabilities (Fig. 9a and Fig. 14a). Instead, the MF profile is characterized by negative fluxes below and positive fluxes above the TIL which show similar magnitudes (Fig. 10). Local values of the MF reach up to $0.034\ \mathrm{kN\,m^{-1}}$ in magnitude which is slightly below the values found for an MW event over New Zealand during DEEPWAVE which where around 0.05 and $0.07\ \mathrm{kN\,m^{-1}}$ in magnitude (Portele et al., 2018). The averaged MF in the stratosphere above the main mountain range (-0.16 Pa) is in the range of to the moderate MW cases of DEEPWAVE [Fig. 5b in (Smith et al., 2016)].

The observed horizontal wavelengths in the vicinity of the TIL were clearly evanescent in the stratosphere (Fig. 5c). This excludes their direct propagation from above followed by their trapping on the TIL similar to Woods and Smith (2011). The presence of interfacial waves that are trapped on inversions and that are likely generated by MWs coming across the inversions (Sachsperger et al., 2017) has not yet been observed at TILs. Linear theory is able to describe the horizontal wavelength and the propagation of the interfacial waves (Vosper, 2004; Sachsperger et al., 2015, 2017). However, the amplitudes depend on the energy source, which is better described by hydraulic theory than by traditional linear models (Sachsperger et al., 2017). The traditional linear models link the energy source to the topography which is inaccurate for interfacial waves (especially for large amplitudes) because of nonlinear effects. Sachsperger et al. (2017) included the nonlinear effects in their model for the amplitudes of interfacial waves on the boundary-layer inversion by assuming that the interfacial waves originate at the density

315 interface further aloft in the interior of the fluid and the energy source for these non-hydrostatic lee wave train is the energy convergence at an internal jump between two fluid layers of different densities.

The determined wave properties (observations) match those of interfacial waves (simulations) for which stability and wind conditions above the inversion determine the horizontal scales of the waves (Vosper, 2004; Sachsperger et al., 2015). The performed simulations show that the presence of the TIL is crucial in producing the trapped waves at tropopause altitude and

320 vertical wind shear by the main mountain wave was not sufficient in this case (Fig. 14a). However, the amplitudes of the interfacial waves were underestimated compared to the upward propagating mountain waves in the simulations. This can have several reasons. The amplitudes of interfacial waves depend on the amount of energy provided by the main wave source at the interface and the acting nonlinear processes (Sachsperger et al., 2017). It was not yet investigated how the interaction and generation processes depend on the model resolution and if the amplitudes increase with increasing resolution. The simulations were only

325 2-dimensional so they cannot capture effects of the fully 3-dimensional mountain range. Moreover, potential additional energy input by downward propagating larger scale waves from stratospheric sources (e.g., polar night jet (Dörnbrack et al., 2018)) are not included in the simulations. The evaluation of these effects and the assessment of their sensitivities require additional extensive model simulations which are beyond the scope of this paper and can be addressed in a future study.

5   Conclusions

330 The unique combination of observations from coordinated airborne in-situ and lidar measurements and idealized large-eddy simulations revealed the occurrence of interfacial waves on the tropopause inversion during an MW event over Southern Scandinavia on 28 January 2016. Such interfacial waves have already been observed on boundary-layer inversions but their concept has not been applied to tropopause inversions so far.

Strong shear induced by the main mountain wave can cause Kelvin-Helmholtz instabilities which results in similar patterns

335 in the vertical velocity field (Mahalov et al., 2011). Although the horizontal scales are around ten kilometers, which is similar to T-REX observations (Smith et al., 2008; Woods and Smith, 2010), neither Kelvin-Helmholtz instability nor downward propagation of secondary GWs generated by MW breaking in the middle stratosphere can explain our observations. The vertical shear was not as pronounced as during the T-REX case (Mahalov et al., 2011) because the tropopause jet was not well established over Southern Scandinavia on 28 January 2016. The wind speed influenced by the large scale mountain wave was

340 only between $10\,\mathrm{m\,s^{-1}}$ and $40\,\mathrm{m\,s^{-1}}$. The stratospheric critical horizontal wavelengths calculated from co-located radiosonde measurements are larger than the observed scales in the UTLS region which would hinder their direct downward propagation from a breaking region located higher up.

Our idealized simulations revealed that interfacial waves can occur also on tropopause inversions similar to boundary layer inversions. Our analyses of the horizontal- and altitude-resolved airborne observations revealed that they actually do occur. As

345 predicted by linear theory, the horizontal scale of those waves is determined by the wind and stability conditions above the inversion. They are found downstream of the main mountain peaks and their characteristic MF profile (negative fluxes below and positive fluxes above the inversion) clearly distinguishes from the MF profile of a Kelvin-Helmholtz instability.

Data availability. HALO and Falcon data is available on HALO-Database (https://halo-db.pa.op.dlr.de/mission/3). ECMWF data is available in the MARS archive (https://apps.ecmwf.int/archive-catalogue/). EULAG simulation data is available on the

350   ftp-server (ftp://ftp.pa.op.dlr.de/pub/gisinger/ACP_EULAG_2020/).

Author contributions. S. Gisinger performed the large-eddy simulations and prepared the manuscript with contributions from all co-authors. J. Wagner did the analyses of the meteorological conditions and the aircraft insitu data. B. Witschas did the analyses of the lidar data.

Competing interests. The authors declare that they have no conflict of interest.

Acknowledgements. This research was funded by the German research initiative "Role of the Middle Atmosphere in Climate (ROMIC/01LG1206A)"

355   funded by the German Ministry of Research and Education in the project "Investigation of the life cycle of gravity waves (GW-LCYCLE)" and by the Deutsche Forschungsgemeinschaft (DFG) via the Project MS-GWaves (GW TP/DO 1020/9 1). We thank the PIs and all participants of the GW-LCYCLE II campaign, in particular, Prof. Markus Rapp and Dr. Andreas Dörnbrack for input and discussions. We thank Dr. Stephan Rahm and Dr. Martin Wirth for providing the lidar data and Martina Bramberger and Tanja Portele for sharing their code and knowledge for the in-situ data analyses. Access to the ECMWF data was possible through the special project "HALO Mission Support

360   System". Computational resources for EULAG simulations were provided by DKRZ. Radiosonde data were downloaded form the public archive of the University of Wyoming.

References

Achatz, U., Klein, R., and Senf, F.: Gravity waves, scale asymptotics and the pseudo-incompressible equations, Journal of Fluid Mechanics, 663, 120–147, https://doi.org/10.1017/S0022112010003411, 2010.

365 Baines, P. G.: Topographic effects in stratified flows, Cambridge University Press, 1 edn., 1995.

Bögel, W. and Baumann, R.: Test and Calibration of the DLR Falcon Wind Measuring System by Maneuvers, Journal of Atmospheric and Oceanic Technology, 8, 5–18, https://doi.org/10.1175/1520-0426(1991)008<0005:TACOTD>2.0.CO;2, https://doi.org/10.1175/1520-0426(1991)008<0005:TACOTD>2.0.CO;2, 1991.

Birner, T.: Fine-scale structure of the extratropical tropopause region, J. Geophys. Res. Atmos., 111, D04104,

370 https://doi.org/10.1029/2005JD006301, 2006.

Bramberger, M., Dörnbrack, A., Wilms, H., Gemsa, S., Raynor, K., and Sharman, R.: Vertically Propagating Mountain Waves—A Hazard for High-Flying Aircraft?, Journal of Applied Meteorology and Climatology, 57, 1957–1975, https://doi.org/10.1175/JAMC-D-17-0340.1, https://doi.org/10.1175/JAMC-D-17-0340.1, 2018.

Chouza, F., Reitebuch, O., Groß, S., Rahm, S., Freudenthaler, V., Toledano, C., and Weinzierl, B.: Retrieval of aerosol backscatter and

375 extinction from airborne coherent Doppler wind lidar measurements, Atmos. Meas. Tech., 8, 2909–2926, https://doi.org/10.5194/amt-8-2909-2015, 2015.

Chouza, F., Witschas, B., and Reitebuch, O.: Heterodyne high-spectral-resolution lidar, Applied optics, 56, 8121–8134, 2017.

Cruette, D.: Experimental study of mountain lee"waves by means of satellite photographs and aircraft measurements, Tellus, 28, 499–523, https://doi.org/10.3402/tellusa.v28i6.11318, https://doi.org/10.3402/tellusa.v28i6.11318, 1976.

380 Dörnbrack, A., Gisinger, S., Kaifler, N., Portele, T. C., Bramberger, M., Rapp, M., Gerding, M., Söder, J., Žagar, N., and Jelić, D.: Gravity waves excited during a minor sudden stratospheric warming, Atmospheric Chemistry and Physics, 18, 12915–12931, https://doi.org/10.5194/acp-18-12915-2018, https://www.atmos-chem-phys.net/18/12915/2018/, 2018.

Doyle, J. D. and Jiang, Q.: Observations and numerical simulations of mountain waves in the presence of directional wind shear, Quart. J.

385 Roy. Meteorol. Soc., 132, 1877–1905, https://doi.org/10.1256/qj.05.140, 2006.

Dunkerton, T.: On the Mean Meridional Mass Motions of the Stratosphere and Mesosphere, J. Atmos. Sci., 35, 2325–2333, https://doi.org/10.1175/1520-0469(1978)035<2325:OTMMMM>2.0.CO;2, 1978.

Eckermann, S. D.: Effect of background winds on vertical wavenumber spectra of atmospheric gravity waves, J. Geophys. Res. Atmos., 100, 14097–14112, https://doi.org/10.1029/95JD00987, 1995.

390 Eckermann, S. D. and Marks, C. J.: GROGRAT: A new model of the global propagation and dissipation of atmospheric gravity waves, Advances in Space Research, 20, 1253 – 1256, https://doi.org/https://doi.org/10.1016/S0273-1177(97)00780-1, http://www.sciencedirect.com/science/article/pii/S0273117797007801, coupling and Energetics in the Stratosphere-Mesosphere-Thermosphere- Ionosphere System, 1997.

Eckermann, S. D., Ma, J., Wu, D. L., and Broutman, D.: A three-dimensional mountain wave imaged in satellite radiance

395 throughout the stratosphere: Evidence of the effects of directional wind shear, Quart. J. Roy. Meteorol. Soc., 133, 1959–1975, https://doi.org/10.1002/qj.187, 2007.

Fritts, D. C. and Alexander, J. M.: Gravity wave dynamics and effects in the middle atmosphere, Rev. Geophys., 41, 1003, https://doi.org/10.1029/2001RG000106, 2003.

Fritts, D. C., Smith, R. B., Taylor, M. J., Doyle, J. D., Eckermann, S. D., Dörnbrack, A., Rapp, M., Williams, B. P., Pautet, P.-D.,
Bossert, K., et al.: The Deep Propagating Gravity Wave Experiment (DEEPWAVE): An airborne and ground-based exploration of gravity
wave propagation and effects from their sources throughout the lower and middle atmosphere, Bull. Amer. Meteor. Soc., 97, 425–453,
https://doi.org/10.1175/BAMS-D-14-00269.1, 2016.

Fritts, D. C., Laughman, B., Wang, L., Lund, T. S., and Collins, R. L.: Gravity Wave Dynamics in a Mesospheric Inversion Layer: 1.
Reflection, Trapping, and Instability Dynamics, J. Geophys. Res. Atmos., https://doi.org/10.1002/2017JD027440, 2018.

Giez, A., Mallaun, C., Zöger, M., Dörnbrack, A., and Schumann, U.: Comparison of static pressure from aircraft trailing cone measurements
and numerical weather prediction analysis, AIAA Aviation, https://doi.org/10.2514/6.2016-3707, 2017.

Gill, A. E.: Atmosphere-Ocean Dynamics (International Geophysics Series, Volume 30) 1st Edition, Academic Press, 1982.

Gisinger, S., Dörnbrack, A., Matthias, V., Doyle, J. D., Eckermann, S. D., Ehard, B., Hoffmann, L., Kaifler, B., Kruse, C. G., and Rapp,
M.: Atmospheric Conditions during the Deep Propagating Gravity Wave Experiment (DEEPWAVE), Mon. Weath. Rev., 145, 4249–4275,
https://doi.org/10.1175/MWR-D-16-0435.1, 2017.

Grubišić, V. and Smolarkiewicz, P. K.: The Effect of Critical Levels on 3D Orographic Flows: Linear Regime, J. Atmos. Sci., 54, 1943–1960,
https://doi.org/10.1175/1520-0469(1997)054<1943:TEOCLO>2.0.CO;2, 1997.

Grubišić, V., Doyle, J. D., Kuettner, J., Dirks, R., Cohn, S. A., Pan, L. L., Mobbs, S., Smith, R. B., Whiteman, C. D., Czyzyk, S., Vosper, S.,
Weissmann, M., Haimov, S., Wekker, S. F. J. D., and Chow, F. K.: The Terrain-Induced Rotor Experiment, Bull. Amer. Meteor. Soc., 89,
1513–1533, https://doi.org/10.1175/2008BAMS2487.1, 2008.

Heller, R., Voigt, C., Beaton, S., Dörnbrack, A., Giez, A., Kaufmann, S., Mallaun, C., Schlager, H., Wagner, J., Young, K., and Rapp, M.:
Mountain waves modulate the water vapor distribution in the UTLS, Atmos. Chem. Phys., 17, 14 853–14 869, https://doi.org/10.5194/acp-
17-14853-2017, https://www.atmos-chem-phys.net/17/14853/2017/, 2017.

Kaifler, N., Kaifler, B., Ehard, B., Gisinger, S., Dörnbrack, A., Rapp, M., Kivi, R., Kozlovsky, A., Lester, M., and Liley, B.: Observational
indications of downward-propagating gravity waves in middle atmosphere lidar data, Journal of Atmospheric and Solar-Terrestrial Physics,
162, 16 – 27, https://doi.org/10.1016/j.jastp.2017.03.003, 2017.

Keller, T. L.: Implications of the hydrostatic assumption on atmospheric gravity waves, J. Atmos. Sci., 51, 1915–1929,
https://doi.org/10.1175/1520-0469(1994)051<1915:IOTHAO>2.0.CO;2, 1994.

Krisch, I., Preusse, P., Ungermann, J., Dörnbrack, A., Eckermann, S. D., Ern, M., Friedl-Vallon, F., Kaufmann, M., Oelhaf, H., Rapp, M.,
Strube, C., and Riese, M.: First tomographic observations of gravity waves by the infrared limb imager GLORIA, Atmospheric Chemistry
and Physics, 17, 14 937–14 953, https://doi.org/10.5194/acp-17-14937-2017, https://www.atmos-chem-phys.net/17/14937/2017/, 2017.

Lane, T. P., Reeder, M. J., and Guest, F. M.: Convectively generated gravity waves observed from radiosonde data taken during MCTEX,
Quart. J. Roy. Meteorol. Soc., 129, 1731–1740, https://doi.org/10.1256/qj.02.196, 2003.

Lindzen, R. S.: Turbulence and Stress owing to Gravity-Wave and Tidal Breakdown, J. Geophys. Res. Atmos., 86, 9707–9714,
https://doi.org/10.1029/JC086iC10p09707, 1981.

Lux, O., Lemmerz, C., Weiler, F., Marksteiner, U., Witschas, B., Rahm, S., Schäfler, A., and Reitebuch, O.: Airborne wind lidar observations
over the North Atlantic in 2016 for the pre-launch validation of the satellite mission Aeolus, Atmospheric Measurement Techniques, 11,
3297–3322, 2018.

Mahalov, A., Moustaoui, M., and Grubišić, V.: A numerical study of mountain waves in the upper troposphere and lower stratosphere,
Atmospheric Chemistry and Physics, 11, 5123–5139, https://doi.org/10.5194/acp-11-5123-2011, https://www.atmos-chem-phys.net/11/
5123/2011/, 2011.

Mallaun, C., Giez, A., and Baumann, R.: Calibration of 3-D wind measurements on a single-engine research aircraft, Atmos. Meas. Tech., 8, 3177–3196, https://doi.org/10.5194/amt-8-3177-2015. ISSN 1867-1381, 2015.

Marksteiner, U., Lemmerz, C., Lux, O., Rahm, S., Schäfler, A., Witschas, B., and Reitebuch, O.: Calibrations and wind observations of an airborne direct-detection wind LiDAR supporting ESA's Aeolus mission, Remote Sensing, 10, 2056, 2018.

Oelhaf, H., Sinnhuber, B.-M., Woiwode, W., Bönisch, H., Bozem, H., Engel, A., Fix, A., Friedl-Vallon, F., Grooß, J.-U., Hoor, P., Johansson, S., Jurkat-Witschas, T., Kaufmann, S., Krämer, M., Krause, J., Kretschmer, E., Lörks, D., Marsing, A., Orphal, J., Pfeilsticker, K., Pitts, M., Poole, L., Preusse, P., Rapp, M., Riese, M., Rolf, C., Ungermann, J., Voigt, C., Volk, C. M., Wirth, M., Zahn, A., and Ziereis, H.: POLSTRACC: Airborne Experiment for Studying the Polar Stratosphere in a Changing Climate with the High Altitude and Long Range Research Aircraft (HALO), Bulletin of the American Meteorological Society, 100, 2634–2664, https://doi.org/10.1175/BAMS-D-18-0181.1, https://doi.org/10.1175/BAMS-D-18-0181.1, 2019.

Plougonven, R. and Zhang, F.: Internal gravity waves from atmospheric jets and fronts, Rev. Geophys., 52, 33–76, https://doi.org/10.1002/2012RG000419, 2014.

Podglajen, A., Hertzog, A., Plougonven, R., and Legras, B.: Lagrangian temperature and vertical velocity fluctuations due to gravity waves in the lower stratosphere, Geophysical Research Letters, 43, 3543–3553, https://doi.org/10.1002/2016GL068148, https://agupubs.onlinelibrary.wiley.com/doi/abs/10.1002/2016GL068148, 2016.

Portele, T. C., Dörnbrack, A., Wagner, J. S., Gisinger, S., Ehard, B., Pautet, P.-D., and Rapp, M.: Mountain-Wave Propagation under Transient Tropospheric Forcing: A DEEPWAVE Case Study, Monthly Weather Review, 146, 1861–1888, https://doi.org/10.1175/MWR-D-17-0080.1, https://doi.org/10.1175/MWR-D-17-0080.1, 2018.

Prusa, J. M., Smolarkiewicz, P. K., and Garcia, R. R.: Propagation and Breaking at High Altitudes of Gravity Waves Excited by Tropospheric Forcing, J. Atmos. Sci., 53, 2186–2216, https://doi.org/10.1175/1520-0469(1996)053<2186:PABAHA>2.0.CO;2, 1996.

Prusa, J. M., Smolarkiewicz, P. K., and Wyszogrodzki, A. A.: EULAG, a computational model for multiscale flows, Computers & Fluids, 37, 1193 – 1207, https://doi.org/10.1016/j.compfluid.2007.12.001, 2008.

Queney, P.: The problem of air flow over mountains: a summary of theoretical studies, Bull. Am. Meteorol. Soc., 29, 16–26, 1948.

Ralph, F. M., Neiman, P. J., Keller, T. L., Levinson, D., and Fedor, L.: Observations, simulations, and analysis of nonstationary trapped lee waves, J. Atmos. Sci., 54, 1308–1333, https://doi.org/10.1175/1520-0469(1997)054<1308:OSAAON>2.0.CO;2, 1997.

Sachsperger, J., Serafin, S., and Grubišić, V.: Lee Waves on the Boundary-Layer Inversion and Their Dependence on Free-Atmospheric Stability, Front. Earth Sci., 3, 70, https://doi.org/10.3389/feart.2015.00070, 2015.

Sachsperger, J., Serafin, S., Grubišić, V., Stiperski, I., and Paci, A.: The amplitude of lee waves on the boundary-layer inversion, Quarterly Journal of the Royal Meteorological Society, 143, 27–36, https://doi.org/10.1002/qj.2915, https://rmets.onlinelibrary.wiley.com/doi/abs/10.1002/qj.2915, 2017.

Sato, K., Watanabe, S., Kawatani, Y., Tomikawa, Y., Miyazaki, K., and Takahashi, M.: On the origins of mesospheric gravity waves, Geophys. Res. Lett., 36, L19 801, https://doi.org/10.1029/2009GL039908, 2009.

Schäfler, A., Craig, G., Wernli, H., Arbogast, P., Doyle, J. D., McTaggart-Cowan, R., Methven, J., Rivière, G., Ament, F., Boettcher, M., et al.: The North Atlantic waveguide and downstream impact experiment, Bulletin of the American Meteorological Society, 99, 1607–1637, 2018.

Schmugge, T. J., Abrams, M. J., Kahle, A. B., Yamaguchi, Y., and Fujisada, H.: Advanced Spaceborne Thermal Emission and Reflection Radiometer (ASTER), Proc. SPIE Remote Sensing for Agriculture, Ecosystems, and Hydrology IV, 4879, https://doi.org/10.1117/12.469693, https://doi.org/10.1117/12.469693, 2003.

475 Scorer, R.: Theory of waves in the lee of mountains, Quart. J. Roy. Meteorol. Soc., 75, 41–56, 1949.

Sharman, R., Trier, S., Lane, T., and Doyle, J.: Sources and dynamics of turbulence in the upper troposphere and lower stratosphere: A review, Geophys. Res. Lett., 39, https://doi.org/10.1029/2012GL051996, 2012.

Shibuya, R., Sato, K., Tsutsumi, M., Sato, T., Tomikawa, Y., Nishimura, K., and Kohma, M.: Quasi-12 h inertia–gravity waves in the lower mesosphere observed by the PANSY radar at Syowa Station (39.6° E, 69.0° S), Atmospheric Chemistry and Physics, 17, 6455–6476,
480 https://doi.org/10.5194/acp-17-6455-2017, https://www.atmos-chem-phys.net/17/6455/2017/, 2017.

Smith, R. B.: The influence of mountains on the atmosphere, Adv. Geophys., 21, 87–230, https://doi.org/10.1016/S0065-2687(08)60262-9, 1979.

Smith, R. B. and Kruse, C. G.: Broad-Spectrum Mountain Waves, J. Atmos. Sci., 74, 1381–1402, https://doi.org/10.1175/JAS-D-16-0297.1, 2017.

485 Smith, R. B., Woods, B. K., Jensen, J., Cooper, W. A., Doyle, J. D., Jiang, Q., and Grubišić, V.: Mountain Waves Entering the Stratosphere, J. Atmos. Sci., 65, 2543–2562, https://doi.org/10.1175/2007JAS2598.1, 2008.

Smith, R. B., Nugent, A. D., Kruse, C. G., Fritt, D. C., Doyle, J. D., Eckermann, S. D., Taylor, M. J., Dörnbrack, A., Uddstrom, M., Cooper, W., Romashkin, P., Jensen, J., and Beaton, S.: Stratospheric gravity wave fluxes and scales during DEEPWAVE, J. Atmos. Sci., 73, 2851–2869, https://doi.org/10.1175/JAS-D-15-0324.1, 2016.

490 Smolarkiewicz, P. K., Margolin, L. G., and Wyszogrodzki, A. A.: A Class of Nonhydrostatic Global Models, Journal of the Atmospheric Sciences, 58, 349–364, https://doi.org/10.1175/1520-0469(2001)058<0349:ACONGM>2.0.CO;2, 2001.

Sutherland, B. R.: Internal Gravity Waves 1st Edition, Cambridge University Press, 2010.

Torrence, C. and Compo, G. P.: A practical guide to wavelet analysis, Bull. Amer. Meteor. Soc., 79, 61–78, https://doi.org/10.1175/1520-0477(1998)079<0061:APGTWA>2.0.CO;2, 1998.

495 Vadas, S. L., Fritts, D. C., and Alexander, M. J.: Mechanism for the Generation of Secondary Waves in Wave Breaking Regions, J. Atmos. Sci., 60, 194–214, https://doi.org/10.1175/1520-0469(2003)060<0194:MFTGOS>2.0.CO;2, 2003.

Vosper, S.: Inversion effects on mountain lee waves, Quart. J. Roy. Meteorol. Soc., 130, 1723–1748, https://doi.org/10.1256/qj.03.63, 2004.

Wirth, M., Fix, A., Mahnke, P., Schwarzer, H., Schrandt, F., and Ehret, G.: The airborne multi-wavelength water vapor differential absorption lidar WALES: system design and performance, Appl. Phys. B, 96, 201–213, 2009.

500 Witschas, B., Rahm, S., Dörnbrack, A., Wagner, J. S., and Rapp, M.: Airborne wind lidar measurements of vertical and horizontal winds for the investigation of orographically induced gravity waves, J. Atmos. Oceanic Technol., 34, 1371–1386, https://doi.org/10.1175/JTECH-D-17-0021.1, 2017.

Witschas, B., Lemmerz, C., Geiß, A., Lux, O., Marksteiner, U., Rahm, S., Reitebuch, O., and Weiler, F.: First validation of Aeolus wind observations by airborne Doppler Wind Lidar measurements, Atmospheric Measurement Techniques Discussions, 2020, 1–23,
505 https://doi.org/10.5194/amt-2019-432, https://www.atmos-meas-tech-discuss.net/amt-2019-432/, 2020.

Witschas, B., Rahm, S., Wagner, J., and Gisinger, S.: Airborne measurements of gravity wave momentum flux by means of a coherent wind lidar, Atmospheric Measurement Techniques Discussions, in preparation.

Woods, B. K. and Smith, R. B.: Energy Flux and Wavelet Diagnostics of Secondary Mountain Waves, J. Atmos. Sci., 67, 3721–3738, https://doi.org/10.1175/2009JAS3285.1, 2010.

510 Woods, B. K. and Smith, R. B.: Short-Wave Signatures of Stratospheric Mountain Wave Breaking, Journal of the Atmospheric Sciences, 68, 635–656, https://doi.org/10.1175/2010JAS3634.1, https://doi.org/10.1175/2010JAS3634.1, 2011.

Wright, C. J., Hindley, N. P., Hoffmann, L., Alexander, M. J., and Mitchell, N. J.: Exploring gravity wave characteristics in 3-D using a novel S-transform technique: AIRS/Aqua measurements over the Southern Andes and Drake Passage, Atmospheric Chemistry and Physics, 17, 8553–8575, https://doi.org/10.5194/acp-17-8553-2017,

515   https://www.atmos-chem-phys.net/17/8553/2017/, 2017.

Wurtele, M., Sharman, R., and Keller, T.: Analysis and simulations of a troposphere–stratosphere gravity wave model. Part I, J. Atmos. Sci., 44, 3269–3281, https://doi.org/10.1175/1520-0469(1987)044<3269:AASOAT>2.0.CO;2, 1987.

Wurtele, M., Sharman, R., and Datta, A.: Atmospheric lee waves, Annu. Rev. Fluid Mech., 28, 429–476, https://doi.org/10.1146/annurev.fl.28.010196.002241, 1996.
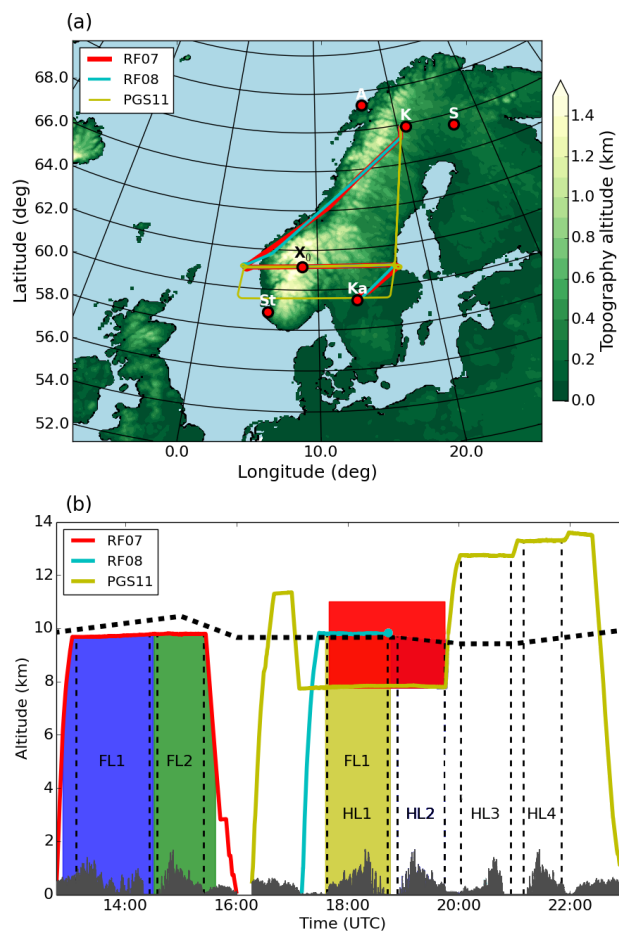
Figure 1. (a) Topographic map of Scandinavia and area of operation of IOP 6 during the GW-LCYCLE II campaign. The coloured lines indicate Falcon (RF07 and RF08) and HALO (PGS11) flight tracks. The red dots mark the position of Andenes (A), Kiruna (K), Sodankylä (S), Karlstad (Ka) and Stavanger (St). The location of the highest mountain peak on the cross-mountain flight legs is marked with X_0. Flight altitudes of Falcon and HALO are shown in (b). Falcon flight legs RF07 FL2 and RF08 FL1 and HALO flight legs PGS11 HL1, HL2 and HL4 are cross-mountain flights through X_0, which are analyzed in this study. Colour shaded areas mark regions covered by the upward looking HALO water vapour lidar WALES (red) and the downward looking Falcon Doppler wind lidar in scanning (blue), nadir (green) and flux mode (yellow). The temporal evolution of the ECMWF thermal tropopause height at point X_0 is indicated with the thick dashed line.
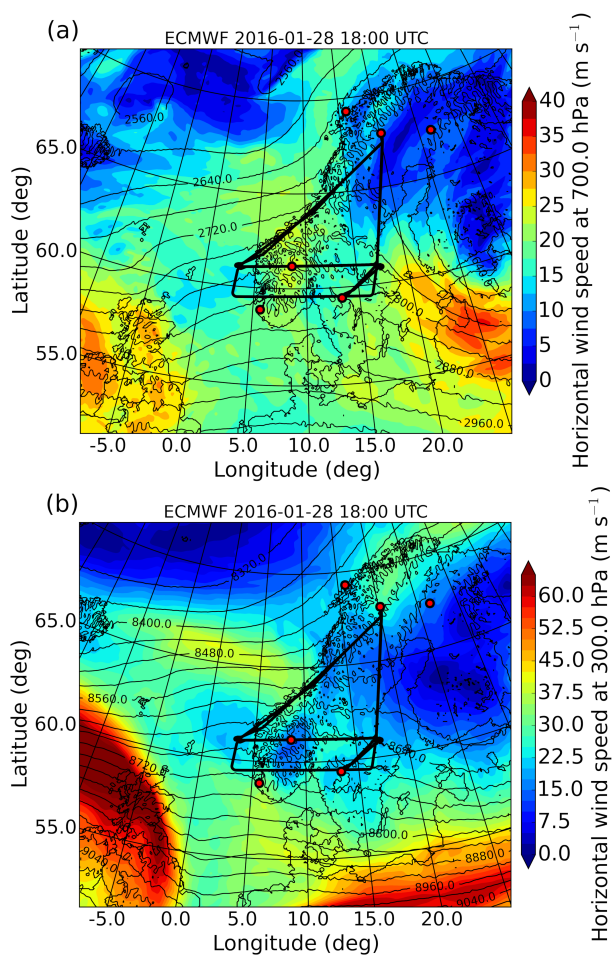
Figure 2. Meteorological maps of horizontal wind speed and geopotential height (black contour lines) at (a) 700 hPa and (b) 300 hPa at 18 UTC on 28 January 2016 obtained from the ECMWF model. Black lines indicate flight legs of the three research flights and red dots mark the same locations as in Figure 1.
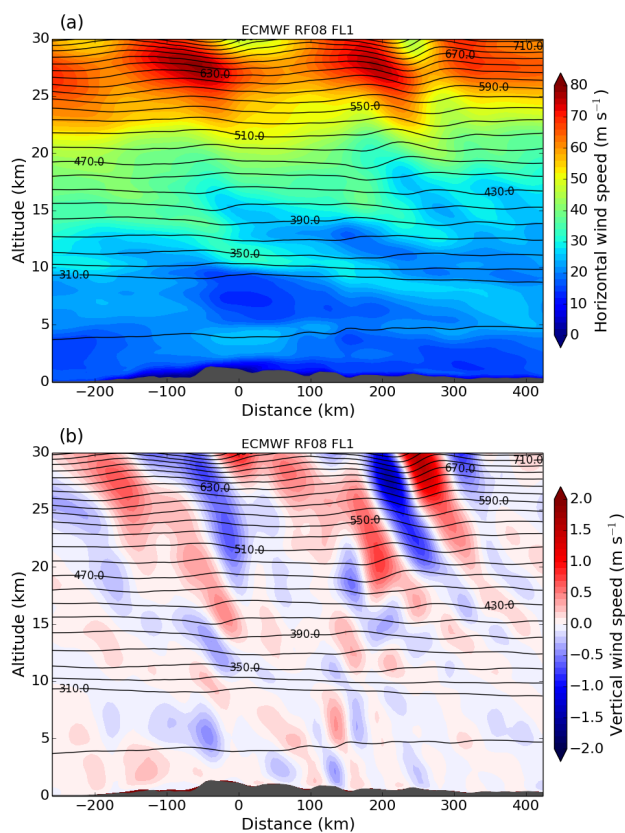
Figure 3. ECMWF vertical cross sections of (a) horizontal wind speed and (b) vertical wind speed interpolated in time and horizontal space along flight leg RF08 FL1. Black contour lines indicate potential temperature with an interval of 20 K. The cross section distance is centered at X_0 (see Fig. 1).
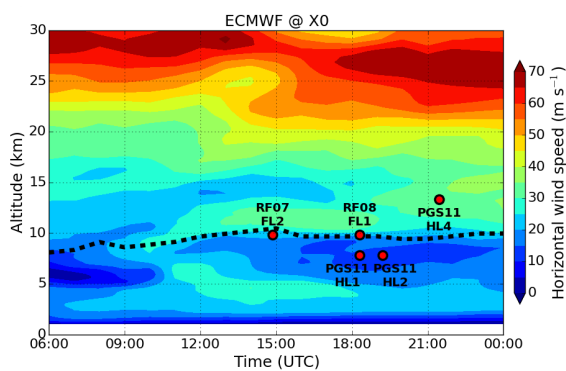
Figure 4. ECMWF time-height section of horizontal wind speed at point X_0. The black dashed line marks the height of the thermal tropopause. Red dots mark the altitudes of HALO and Falcon at point X_0 of the respective flight legs (see also Fig. 1).
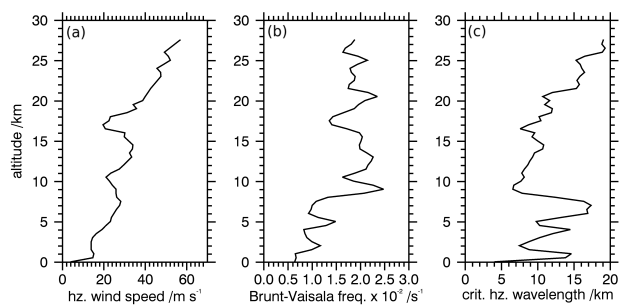
Figure 5. Vertical profiles of (a) horizontal wind speed, (b) Brunt-Vaisala frequency, and (c) critical horizontal wavelength of the radiosonde launched at Stavanger (St) southern Norway (Fig. 1) at 12 UTC on 28 January.
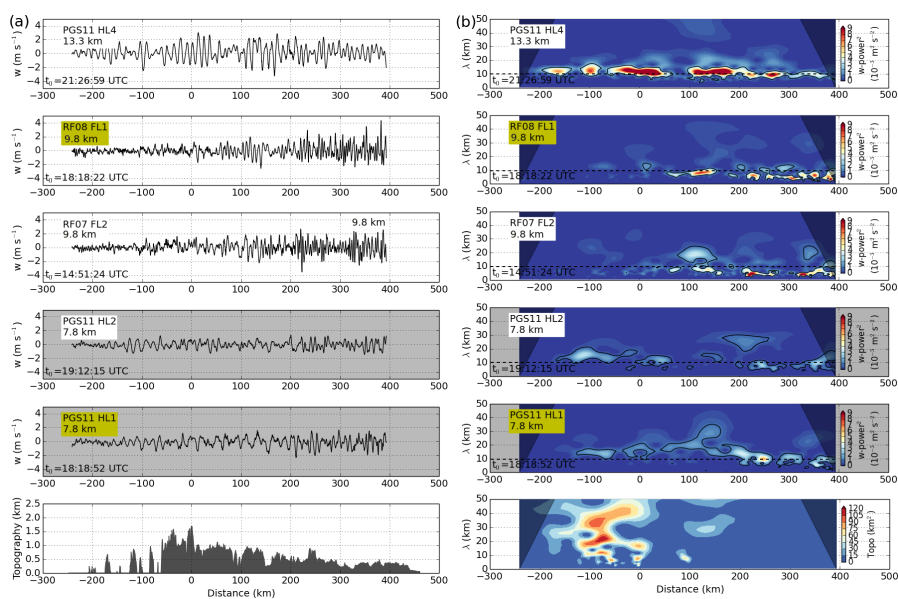
Figure 6. Cross mountain flight legs of Falcon and HALO for (a) in-situ vertical wind and topography and (b) corresponding wavelets of vertical wind. Black contour lines mark regions, which are significant on the 5%-level. The cone of influence is shaded in grey and flight legs, which were located below the tropopause (see labelled mean flight altitudes) are marked with grey background colour. Time t_0 indicates when the aircraft was located at X_0 (see Fig. 1) and shows that PGS11 HL1 and RF08 FL1 (labelled with yellow boxes) took place nearly at the same time (HALO was flying 30 seconds behind Falcon).
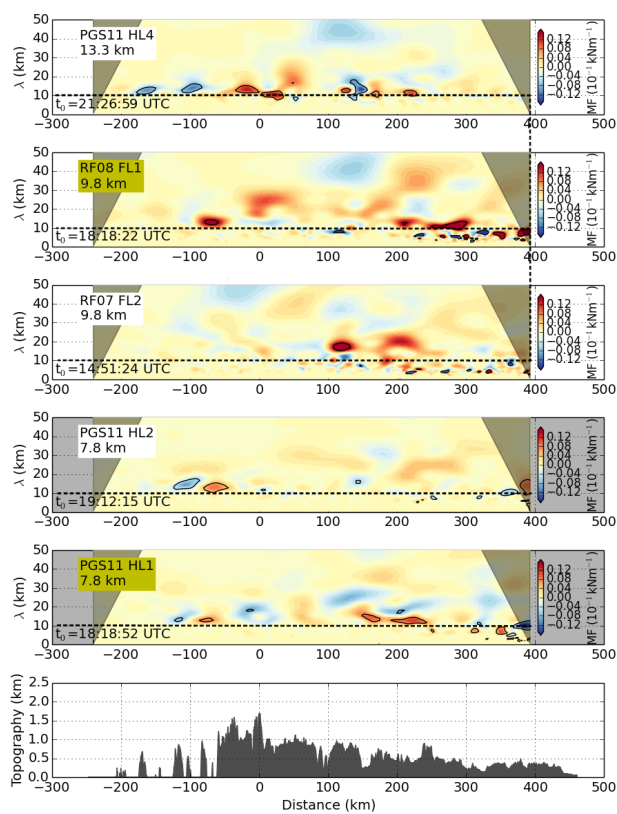
Figure 7. As in Fig. 6b but showing wavelet cospectra of MF ($\rho u'w'$).
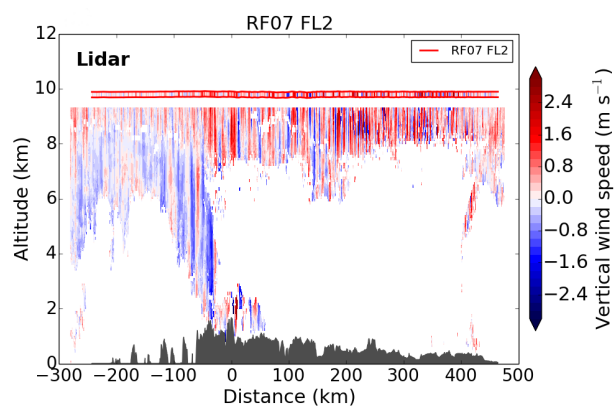
Figure 8. Vertical winds along flight leg RF07 FL2 measured by the DWL and in-situ instruments (marked by red horizontal lines) at flight level by the DLR Falcon.
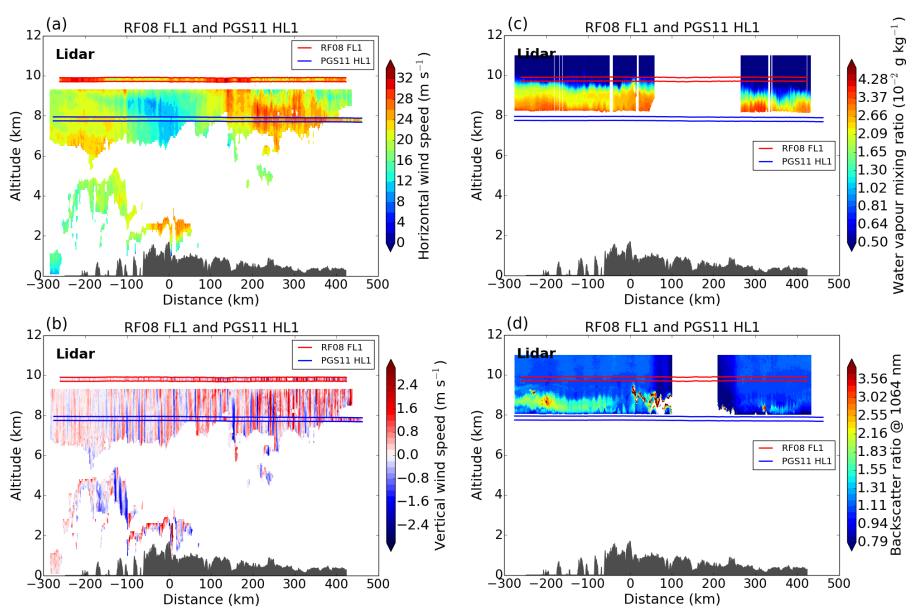
Figure 9. DWL measurements of (a) horizontal wind speed and (b) vertical wind speed and WALES measurements of (c) water vapour mixing ratio and (d) lidar reflectivity along flight leg RF08 FL1/PGS11 HL1 combined with corresponding in-situ measurements of HALO and DLR Falcon at flight level (marked by blue and red horizontal lines).
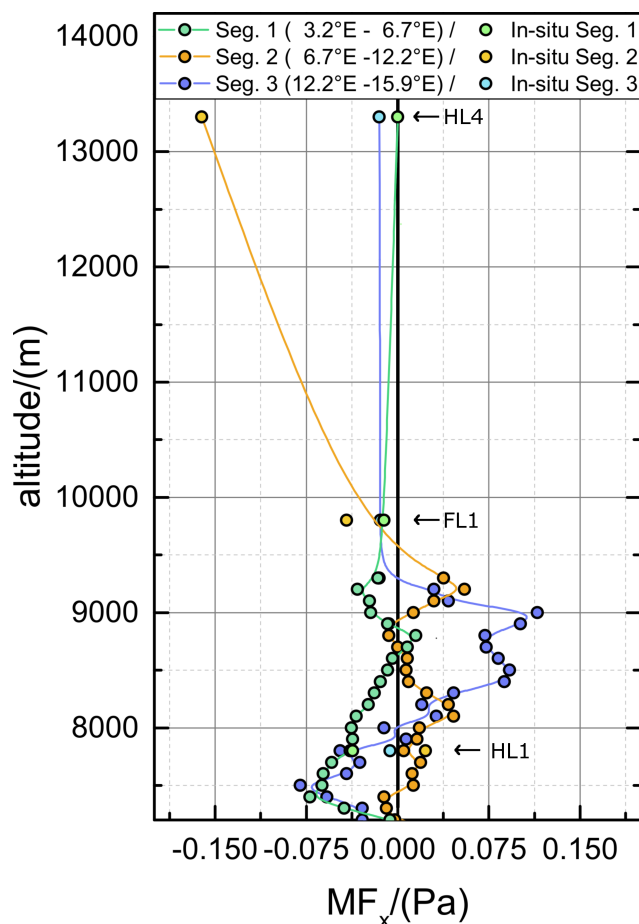
Figure 10. Leg-averaged momentum flux profiles along flight leg RF08 FL1 obtained from DWL and in-situ measurements which include also PGS11 HL1 and HL4. Segment 1 is the upstream part of the leg, segment 2 the part above the main mountain range, and segment 3 the downstream part of the leg. Bold black line separates positive and negative fluxes.
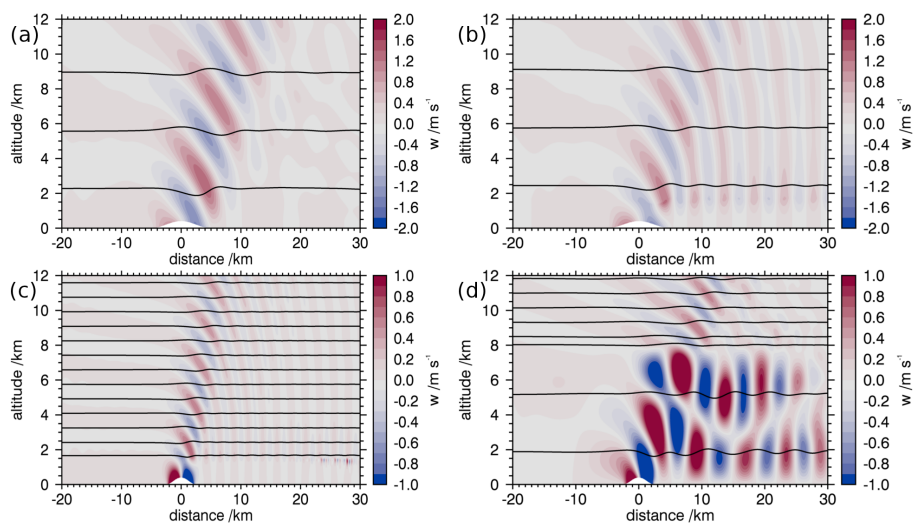
Figure 11. Vertical velocity of the idealized simulations of the cases with (a) a neutral boundary layer without inversion and $N_U = 0.01\,\mathrm{s}^{-1}$ (RUN 1), (b) a neutral boundary layer with an inversion of 3.3 K and $N_U = 0.01\,\mathrm{s}^{-1}$ (RUN 2), (c) a neutral boundary layer with an inversion of 6.6 K and $N_U = 0.02\,\mathrm{s}^{-1}$ (RUN 3), and (d) a stable troposphere ($N = 0.01\,\mathrm{s}^{-1}$) with a TIL of 6.6 K and $N_U = 0.02\,\mathrm{s}^{-1}$ (RUN 4).
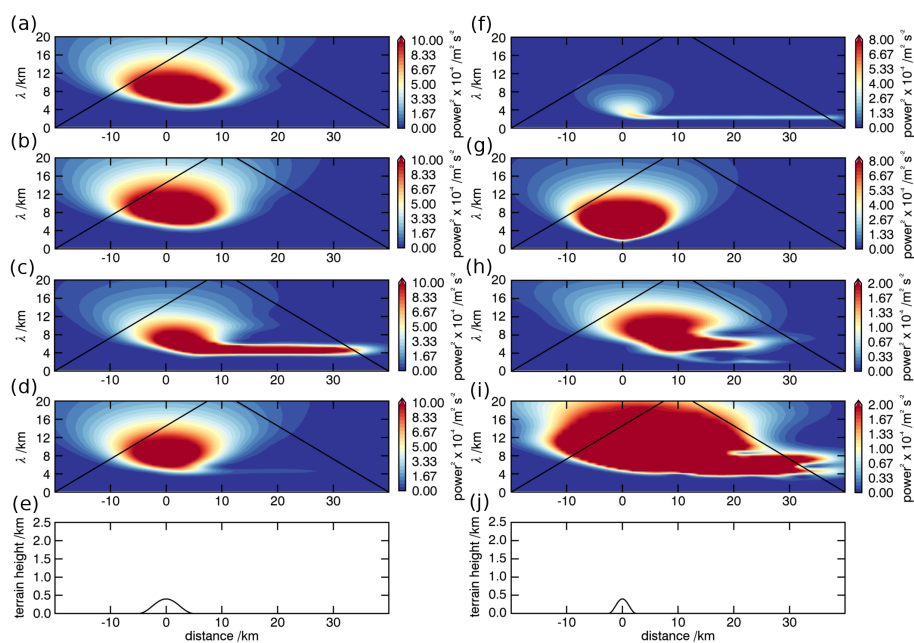
Figure 12. Wavelet spectra of the vertical velocity of the idealized simulations shown in Fig. 11 in the vicinity of (a, c, f, h) and below (b, d, g, i) the top of the boundary layer or the inversion layer. e and j show the idealized terrain. (a, b) is for a neutral boundary layer without inversion and $N_U = 0.01 \text{ s}^{-1}$ (RUN 1), (c, d) for a neutral boundary layer with an inversion of 3.3 K and $N_U = 0.01 \text{ s}^{-1}$ (RUN 2), (f, g) for a neutral boundary layer with an inversion of 6.6 K and $N_U = 0.02 \text{ s}^{-1}$ (RUN 3), and (h, i) for a stable troposphere ($N = 0.01 \text{ s}^{-1}$) with a TIL of 6.6 K and $N_U = 0.02 \text{ s}^{-1}$ (RUN 4).
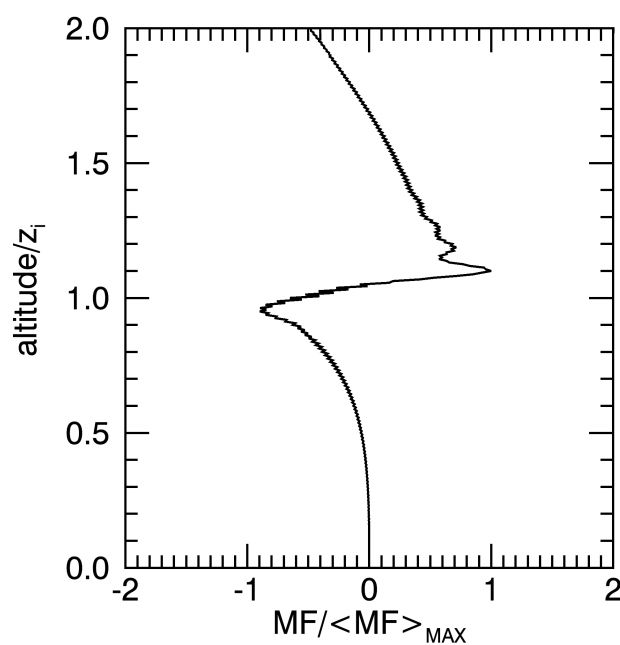
Figure 13. Averaged momentum flux of the interfacial waves on the boundary layer inversion (RUN 2: 3.3 K and $N_U = 0.01 \ \text{s}^{-1}$, Fig. 11b, Fig. 12c) downstream of the idealized mountain (10-30 km horizontal distance). Values are normalized by the maximum flux in the vicinity of the inversion and given as a function of normalized altitude (z_i is the altitude of the inversion).
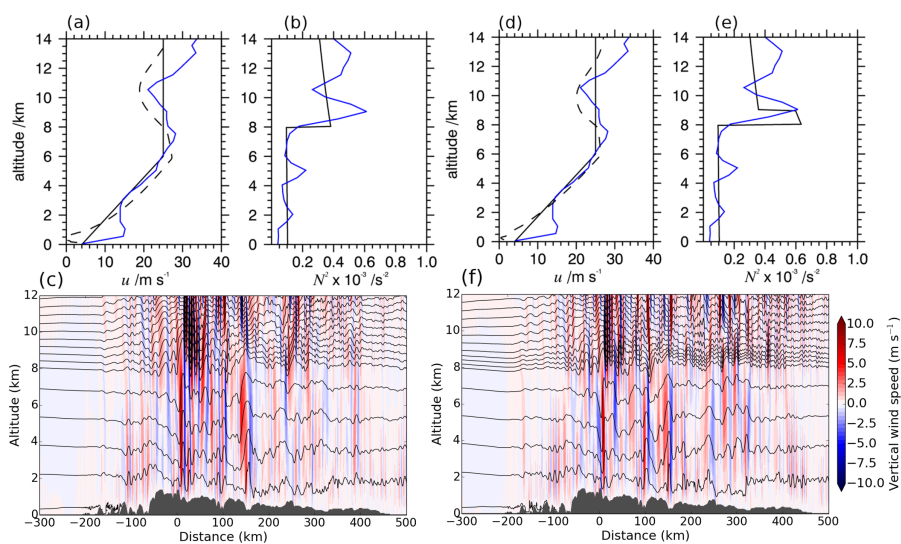
Figure 14. Initial profiles (black solid) and vertical velocity for the simulations with more realistic terrain without TIL (a-c, RUN 5) and with TIL (d-f, RUN 6). The initial profiles approximate the background conditions over southern Scandinavia on 28 January 2016 (blue profiles show the Stavanger radiosonde data). Negative shear above the tropopause establishes in the course of the simulations (a, d; black dashed, time = 16 h, distance = −150 km).
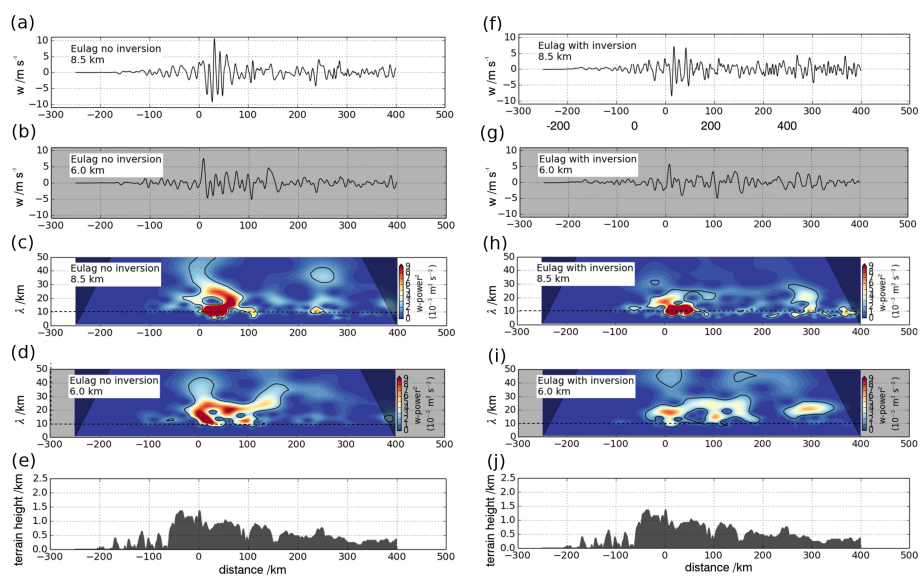
Figure 15. Vertical velocity and corresponding wavelet spectra of the simulations shown in Fig. 14 [left: without TIL (RUN 5), right: with TIL (RUN 6)]. a, c, f, h are at the altitude of the TIL and b, d, g, i below the tropopause. e and j show the terrain in the domain.

Table 1. Mountain width L, static stabilities of the lower and upper layer (N_L,N_U), strength of the inversion ($\Delta\theta$) and inversion height (z_i), upstream wind conditions, and background density of the EULAG simulations.

RUN	L /km	N_L /s^{-1}	N_U /s^{-1}	$\Delta\theta$ /K	z_i /m	U /m s^{-1}	$\bar{\rho} = const.$
1	10	0.00	0.01	0.0	400	8	yes
2	10	0.00	0.01	3.3	1600	8	yes
3	5	0.00	0.02	6.6	1600	8	yes
4	5	0.01	0.02	6.6	8000	8	yes
5	ASTER topo	0.01	0.02	0.0	8000	$4 \rightarrow 25$	no
6	ASTER topo	0.01	0.02	20	8000	$4 \rightarrow 25$	no